Journal of Materials Chemistry C

ROYAL SOCIETY OF CHEMISTRY

PAPER

View Article Online
View Journal

Cite this: DOI: 10.1039/d6tc00067c

In situ electric field X-ray total scattering reveals composition-dependent electromechanical strain mechanisms in $(1-x)BiFe_{2/8}Ti_{3/8}Mg_{3/8}O_3$–$xPbTiO_3$ ceramics†

Brooke N. Richtik, [a] Rachel Beall, [b] Leah Bellcase, [b] Vedika Shah, [b] Tiffany L. Kinnibrugh, [c] Simon Trudel, *[a] Jacob L. Jones [b] and Michelle R. Dolgos *[ad]

Ferroelectric materials find many applications in energy and aerospace industries. A major challenge for ferroelectric materials is maintaining their properties at elevated temperatures. The $(1-x)BiFe_{2/8}Ti_{3/8}Mg_{3/8}O_3$–$xPbTiO_3$ (BFTM–*x*PT) ferroelectric solid solution is a promising candidate for high-temperature applications as it has a high piezoelectric response while also maintaining its ferroelectric phase until a high Curie temperature (T_C) of 650 °C. In this work, we investigate the piezoelectric mechanism in BFTM–*x*PT, a novel high-T_C ferroelectric ceramic. To elucidate the origin of its enhanced piezoelectric performance, relative to other piezoceramics of similar T_C, *in situ* electric field X-ray total scattering experiments were performed. Total scattering combines Bragg scattering (diffraction) and diffuse scattering (pair distribution function), providing insight on various length scales. With information spanning different length scales, extrinsic contributions (*i.e.*, domain wall motion and interphase boundary motion) can be separated from intrinsic contributions (*i.e.*, piezoelectric lattice strain). We show that, for compositions within the morphotropic phase boundary (MPB, $x = 0.325$), the piezoelectric response is dominated by intrinsic piezoelectric lattice strain, whereas outside the MPB ($x = 0.375$) the major component of the piezoelectric response is from extrinsic mechanisms including an electric-field-induced phase transition and tetragonal domain wall motion. This article reveals that the origin of piezoelectric response in BFTM–*x*PT is composition-dependent and shows that high-performance materials may also be located outside the MPB. These findings can help guide material design to optimize properties for specific applications.

Received 8th January 2026,
Accepted 15th March 2026

DOI: 10.1039/d6tc00067c

rsc.li/materials-c

1 Introduction

Piezoelectric materials, which couple mechanical and electrical energy, are widely used in sensors and actuators due to their ability to generate an electric charge under mechanical stress (direct piezoelectric effect) and undergo mechanical deformation under an applied electric field (converse piezoelectric effect).[1] The demand for high-temperature, high-performance sensors and actuators in aerospace and energy industries is increasing rapidly with more systems operating in extreme environments.[2–4] One example being piezoelectric sensors for structural health monitoring to enhance the safety and serviceability of high-temperature systems.[5,6] Currently, lead zirconate titanate (PZT)-based ceramics dominate industrial applications due to their high piezoelectric performance (200–600 pC N^{-1} for $PbZr_{0.52}Ti_{0.48}O_3$, depending on dopants).[7] However, PZT exhibits a low Curie temperature T_C (390 °C for $PbZr_{0.53}Ti_{0.47}O_3$)[8] which prevents its use in high-temperature environments.

[a] Department of Chemistry and Institute for Quantum Science and Technology, University of Calgary, 2500 University Drive NW, Calgary, AB T2N 1N4, Canada. E-mail: trudels@ucalgary.ca
[b] Department of Materials Science and Engineering, North Carolina State University, Raleigh, NC 27695, USA
[c] Advanced Photon Source, Argonne National Laboratory 9700 S Cass Ave, Lemont, IL 60439, USA
[d] Oak Ridge National Laboratory, 1 Bethel Valley Rd, Oak Ridge, TN 37830, USA. E-mail: dolgosmr@ornl.gov

Additionally, growing regulatory pressure to reduce toxicity drives the search for lead-free or lead-reduced alternatives.[9–11] A low-T_C and high-toxicity are two limitations of PZT, and there is a current need for new environmentally friendly piezoelectric materials with high performance and high operating temperature.

A promising candidate for high-temperature piezoelectric applications is a solid solution between two perovskite structures: $BiFe_{2/8}Ti_{3/8}Mg_{3/8}O_3$ (space group: *R3c*) and $PbTiO_3$ (space group: *P4mm*), denoted $(1-x)BiFe_{2/8}Ti_{3/8}Mg_{3/8}O_3$–$xPbTiO_3$, or BFTM–*x*PT. The $BiFe_{2/8}Ti_{3/8}Mg_{3/8}O_3$ end member plays a key role in the enhanced properties of BFTM–*x*PT owing to the presence of Bi^{3+} on the A-site and its high T_C. Incorporating Bi^{3+} on the A-site is advantageous because, like Pb^{2+}, it possesses a $6s^2$ lone pair that hybridizes with oxygen anions, promoting strong structural distortions. However, stabilizing Bi^{3+} on the perovskite A-site is often challenging due to its small ionic radius (Bi^{3+}_{XII} = 1.34 Å).[12] In $BiFe_{2/8}Ti_{3/8}Mg_{3/8}O_3$, the presence of three B-site cations of different valences (Fe^{3+}, Ti^{4+} and Mg^{2+}) provides a flexible framework that accommodates the small Bi^{3+} cation within the large A-site cavity. Additionally, $BiFe_{2/8}Ti_{3/8}Mg_{3/8}O_3$ exhibits a low Goldschmidt tolerance factor,[13] a key feature that stabilizes the non-centrosymmetric phase at high temperature.[12] Consequently, $BiFe_{2/8}Ti_{3/8}Mg_{3/8}O_3$ has a high T_C of 760 °C.[14]

When $BiFe_{2/8}Ti_{3/8}Mg_{3/8}O_3$ is combined with $PbTiO_3$ it forms a solid solution.[15] The piezoelectric coefficient (d_{33}) of BFTM–*x*PT improves from a near negligible response of 0.6 (x = 0) to 145 pC N^{-1} (x = 0.375); most importantly, whilst maintaining a high T_C of 650 °C (x = 0.325).[15,16] Furthermore, the lead content is reduced from 60 wt% in PZT to ~22 wt% in BFTM–*x*PT. Notably, BFTM–*x*PT exhibits a macroscopic strain response of 0.19% at composition x = 0.325,[15] which matches the strain performance of commercial PZT-5H (0.18%).[17] It also exceeds the d_{33} of high-T_C ceramics with similar Curie temperatures.[15] For example, 1% MnO-doped $0.25BiFeO_3$–$0.75BaTiO_3$ exhibits a T_C of 619 °C and a d_{33} of 117 pC N^{-1}.[18] Thus, BFTM–*x*PT is a promising material for commercialization as it has high piezoelectric performance, reduced toxicity, and a high T_C.

Our initial report of BFTM–*x*PT showed that the piezoelectric properties of BFTM–*x*PT are highly sensitive to $PbTiO_3$ concentration,[15] and the low-field (d_{33}) and high-field (d^*_{33}) piezoelectric coefficients are plotted in Fig. 1. At the MPB (x = 0.325), the high-field piezoelectric coefficient (d^*_{33}) reaches 190 pm V^{-1}, exceeding the low-field value of 100 pC N^{-1}. In contrast, outside the MPB (x = 0.375) the high-field d^*_{33} is 150 pm V^{-1}, but the low-field d_{33} is surprisingly higher than the MPB at 145 pC N^{-1}. The large contrast in magnitude of d_{33} and d^*_{33} suggests that the MPB composition (x = 0.325) operates through a different mechanism than compositions outside the MPB (x = 0.375), despite only a 5% increase in $PbTiO_3$. Furthermore, the large discrepancy between the low- and high-field d_{33} in x = 0.325 suggests that there may be a cooperative mechanism under high fields, leading to improved strain within the MPB.

In our previous study,[19] we performed a detailed investigation of the average structure of BFTM–*x*PT using combined Rietveld refinements against X-ray and neutron diffraction

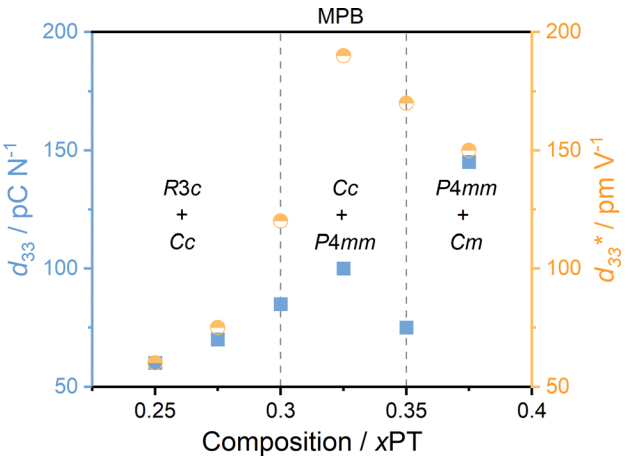

Fig. 1 Low- (d_{33}) and high-field (d^*_{33}) piezoelectric coefficients for BFTM–*x*PT (x = 0.250–0.375) including the space group assignment as determined from previous work.[19] Piezoelectric coefficients were obtained from Rowe *et al.*[15]

data. Our previous study revealed that compositions with x = 0.300–0.350 were best described by mixed-phase models, with monoclinic *Cc* as the major phase and tetragonal *P4mm* as the minor phase.[19] At x = 0.375, the structure transitions to a two-phase coexistence in which *P4mm* becomes the major phase and monoclinic space group *Cm* emerges as the minor phase.[19] The monoclinic space groups *Cc* and *Cm* are nearly isostructural, differing only by the nature of their octahedral tilt systems (*Cc* is tilted and *Cm* is non-tilted). The suppression of octahedral tilting at x = 0.375 may partly explain the larger d_{33} observed relative to the compositions at the MPB, as octahedral tilting is known to hinder the piezoelectric response.[20] However, the description of the average structure alone does not capture the high-field electromechanical behaviour. While the low-symmetry monoclinic phase and the presence of multi-phase coexistence are known to contribute to the enhanced piezoelectric properties at the morphotropic phase boundary (MPB), the underlying mechanisms governing the exceptional performance under high-field remain unclear. This current study therefore aims to investigate the origin of the piezoelectric response at high electric fields.

Electric-field-induced strain in piezoelectric ceramics generally arises from a combination of three effects: (1) phase transformations; (2) domain wall motion; and (3) piezoelectric lattice strain.[21] The first two contributions are generally referred to as extrinsic, while the latter is an intrinsic contribution. *In situ* electric field total scattering experiments have emerged as a powerful tool to deconvolute the contributions within the overall electromechanical response, and have successfully been used to uncover the mechanism behind several high-performance materials.[22–26] Total scattering encompasses both the Bragg reflections, which arise from long-range crystalline order and provide information about the average structure, as well as the diffuse scattering, which encodes the local, short-range correlations.[27] Considering both length scales is essential, as piezoelectric ceramics often have a complex structure

where the local, short-range structure differs from the long-range average structure, as is the case for $BaTiO_3$.[28,29] Accordingly, total scattering data provides the necessary information on various length scales to determine the mechanism of piezoelectric response.

The aim of this research is to understand the mechanism of piezoelectric response along the compositions within the BFTM–*x*PT solid solution. This work presents *in situ* electric field X-ray total scattering data to uncover the structural changes on the long- and short-range length scale. Phase fraction changes and domain wall motion were investigated through diffraction data, where full Rietveld refinements with a texture model were completed to determine the extent of domain reorientation and phase fraction changes upon application of the electric field. The local structure was analysed by quantifying changes in the pair distribution function. In this article, we show that the mechanism of piezoelectric response differs inside *vs.* outside the MPB. The mechanism outside the MPB (x = 0.375) is predominately extrinsic with both domain wall motion and pseudorhombohedral-to-tetragonal phase transition, while within the MPB intrinsic piezoelectric lattice strain is the main contribution to its piezoelectric response.

2 Experimental

2.1 Sample preparation

Ceramic pellets of BFTM–*x*PT (x = 0.275–0.400) were prepared using conventional solid-state synthesis methods following the procedure previously reported by our group.[15] The pellets were polished to $<$0.5 mm thickness with a mirror finish using a semi-automatic polishing machine (LaboPol-5, Struers) with a series of SiC foils (grits of #800, #1200, and #4000, sequentially). Polished ceramic pellets were cut into bars (0.5 × 0.5 × 5.0 mm) using a low-speed diamond saw (MTI, SYJ-160). Electrodes were then applied to the polished, long face of each ceramic bar using silver conductive paint (SPI supplies). The edges were hand polished to remove any deposited silver paint that could cause an electrical shortage. The painted bars were then sintered in air for 1 h at 600 °C. Cross-sectional field emission scanning electron microscopy (FESEM) (FEI Quanta FEG 250) with accelerating voltage of 20 kV under high vacuum ($<10^{-6}$ Torr) was used to determine the grain size of BFTM–*x*PT (x = 0.275–0.3750) ceramics. The cross-sectional FESEM images were collected on fractured ceramic bars coated with Pt. The cross-sectional FESEM images were collected on fractured ceramic bars coated with Pt. Grain sizes were measured using ImageJ.[30]

2.2 Total scattering experiments

X-ray total scattering data were obtained at ambient temperature at 11-ID-B at the Advanced Photon Source at Argonne National Laboratory. Data were acquired using a PerkinElmer XRD1621 amorphous silicon 2D detector. Diffraction and PDF data were collected with incident energies of 59 and 87 keV, respectively. A cerium dioxide standard was used to calibrate the beam center and the sample-to-detector distance. The sample-to-detector distances were nominally set to 1000 mm for diffraction measurements and 250 mm for PDF measurements. The sample was submerged in an electrically insulating Fluorinert (3M, USA) bath in a Kapton (DuPont, USA) container. The signal from the Fluorinert liquid and Kapton container were collected separately, then subtracted from the total signal. During the collection of PDF data, the sample stage was tilted to 14° towards the incident X-ray beam to minimize the angular variation between the scattering and electric field vectors with respect to the detector plane.[22] An Agilent 33220A function generator (20 MHz function, arbitrary waveform generator) and Matsusada high-voltage power supply (Model AMS-10B2, S/N 046594L) were used to apply an electric field across the sample. Data were collected during the application of the electric field. The field was increased from 0 to 8 kV mm^{-1} in 1 kV mm^{-1} increments, then decreased in 2 kV mm^{-1} steps. Immediately after collecting the total scattering data, the direct piezoelectric effect (d_{33}) of each pellet was measured on a Berlincourt-type d_{33} meter (APC International, Ltd YE2730A) to ensure that successful poling of the sample was achieved.

2.3 Data processing

The GSAS-II software[31] was used to integrate 2D diffraction data, and to calculate the PDFs. The PDF data ($G(r)$) is calculated by performing a Fourier transform of the $S(Q)$ data. The data collected on the 2D-detector were integrated in sectors to separate the contributions of crystallites with their Q_{hkl} vectors in different directions with respect to the electric field. The diffraction data was binned in ±10-degree sectors then integrated to obtain 10 datasets covering a detector region between ϕ = 0–90° where ϕ represents the angle between the integration region and the direction of applied field as shown in Scheme 1.

For the calculated PDFs, data was also binned in ±10-degree sectors, and the datasets at ϕ = 0° (parallel) and ϕ = 90° (perpendicular) were analysed. The Q_{max} was set to 20 Å and

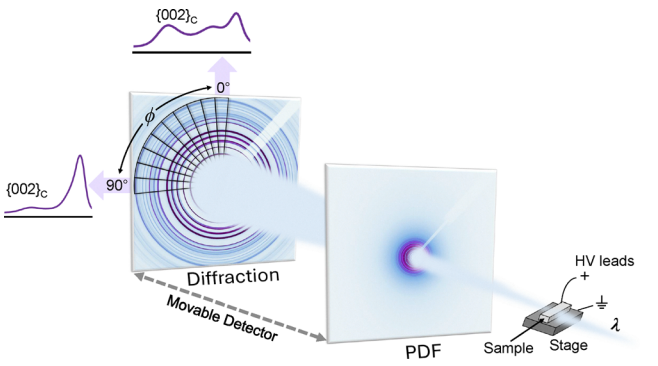

Scheme 1 Experimental set-up of the *in situ* electric field total scattering at 11-ID-B. The sample was mounted on a grounded stage with a high voltage (HV) lead attached. The incident synchrotron X-ray beam (λ) was directed at the sample, and diffracted X-rays were captured by a movable detector, positioned at 250 mm and 1000 mm for collection of pair distribution function data and diffraction data, respectively. For orientational analysis, data were binned by radial angle ϕ relative to the applied field (for ϕ = 0° $Q \parallel E$, and for ϕ = 90° $Q \perp E$).

the Lorch function[32] was applied to suppress additional oscillations in the PDF data caused by the truncation effect during the Fourier transform. Previous work has shown that conventional calculations using the sine Fourier transform of the scattering function $S(Q)$ is adequate to maintain directionality when calculating directional PDFs from directional $S(Q)$.[22]

2.4 Refinements

Texture refinements were performed using Materials Analysis Using Diffraction (MAUD, version 2.9997).[33] The data collected at zero applied field was first analyzed, and then used as a starting model for refinements against the data collected with an applied field. For texture refinements against data collected at applied E-field ($E \neq 0$), the background, lattice parameters, microstructure, atomic coordinates, and isotropic displacement parameters of the cations were refined. The atomic coordinates and isotropic displacement parameters of oxygen anions were fixed to previously reported values.[19] The microstructure was modeled using the Popa line broadening model in conjunction with anisotropic crystallite size and strain for *P*4*mm* and *R*3*m* phases. For the analysis of data collected under an applied electric field, the model was refined against 10 datasets (ϕ = 0–90°). The lattice parameters, atomic positions, and isotropic displacement parameters were fixed to the values obtained from zero-field refinements. A spherical harmonic texture function (order = 4) and a weighted strain orientation distribution function (WSODF)[34] were included to model the electric-field-induced texture and anisotropic microstrain. In all refinements, scale factors, harmonic texture and WSODF parameters were refined for both *P*4*mm* and *R*3*m* phases.

2.5 Intrinsic strain determination

Analysis of the PDF data was completed to calculate the intrinsic piezoelectric lattice strain. The calculation of intrinsic strain from PDF data has been successful in quantifying the local strain in other important systems.[22,23,26,35] The difference between initial data ($G(r)_0$) and the data collected at the highest voltage achieved ($G(r)_{max}$) is represented by $\Delta G(r)$ as defined in eqn (1).

$$\Delta G(r) = G(r)_0 - G(r)_{max} \quad (1)$$

The changes in $\Delta G(r)$ can be quantified by calculating the residual R_Δ, shown in eqn (2).[23]

$$R_\Delta = \frac{\sum_{r}^{r+\Delta} \left| G(r \pm \delta r)_0 - G(r)_E \right|}{\sum_{r}^{r+\Delta} \left| \frac{G(r)_0}{N} \right|} \quad (2)$$

The term R_Δ represents the residual between $G(r)_0$ and $G(r)_E$ (a non-zero applied electric field) calculated between region Δ. The R_Δ value was calculated using a boxcar method with a sampling range (N) of ±1.5 Å and a step size of 1 Å. In eqn (2), $G(r)_0$ is shifted by δr to minimize R_Δ, where δr was varied between −1 to 1 in 0.001 increments. The value of δr that minimizes R_Δ is reported. In other words, δr represents the amount that $G(r)_0$ would have to shift to best represent $G(r)_E$ as a function of distance r. The δr gradient was then obtained by a linear fit of δr for $10 < r < 40$ Å with the $\delta r(0)$-intercept fixed to 0.

3 Results

3.1 Diffraction

The average grain size, determined by cross-sectional FESEM, ranged between 0.8–1.0 μm for BFTM–*x*PT (x = 0.275–0.3750) ceramics with no compositional trend (Fig. S1). The small grain size (≤1 μm) of BFTM–*x*PT is ideal to obtain high-quality diffraction data with even intensity of the Debye Scherrer rings necessary for analysis of *in situ* electric field data. Prior to applying an electric field, diffraction data were collected on a pristine, unpoled pellet. Rietveld refinements were performed on the zero-field data to establish a starting model for subsequent texture refinements of the data collected under applied-field conditions. The crystallographic structure from our previous work[19] served as an initial model for the zero-field refinements. Our previous work reported BFTM–*x*PT to crystallize as a mixed-phase tetragonal + monoclinic material best described by *P*4*mm* + *Cc* for x = 0.300–0.350, and *P*4*mm* + *Cm* when $x \geq 0.375$.[19]

In this present work, the monoclinic phase (either *Cc* or *Cm*) is modeled by a pseudorhombohedral (PR) phase of space group *R*3*m* to simplify the refinements. A simplified approach is adopted since *Cc* and *Cm* are both lower symmetry than *R*3*m* and therefore require more reflections and parameters than can be observed with the resolution of data from an area detector. Following the precedent of an *in situ* electric field diffraction study on $0.40BiScO_3$–$0.6PbTiO_3$, the space group *Cm* was reasonably approximated by space group *R*3*m* due to the structural similarity between the two space groups and the resolution limits of the instrumental setup.[36] Notably, space group *Cc* differs from *Cm* only by the presence of octahedral tilting, a distinction that is difficult to detect by X-ray diffraction due to the weak oxygen scattering relative to heavy cations.[19] Consequently, space group *R*3*m* provides a reasonable, simplified structural model for space group *Cc* as well.

For completeness, Rietveld refinements against x = 0.300 and 0.325 compositions were also completed using *P*4*mm* + *Cc* to compare modeling with the monoclinic phase with space group *Cc* and space group *R*3*m*. The refinements against x = 0.300 using *P*4*mm* + *Cc* and *P*4*mm* + *R*3*m* yielded weighted residual (R_{wp}) of 11.37 and 12.10%, respectively (*cf.* Tables S1–S3). The *P*4*mm* + *R*3*m* results are presented, as the two models have similar quality of fit metrics and employing the same structural description ensures methodological consistency, enabling a reliable trends comparison. However, analysis of the *P*4*mm* + *Cc* model was completed and is included in the SI (Fig. S2–S4, and Table S1). Throughout this paper, space group *R*3*m* will be referred to as the "pseudorhombohedral (PR) phase" as it represents the low-symmetry rhombohedral-like phase, and the tetragonal *P*4*mm* phase will be labeled with "T". All crystallographic

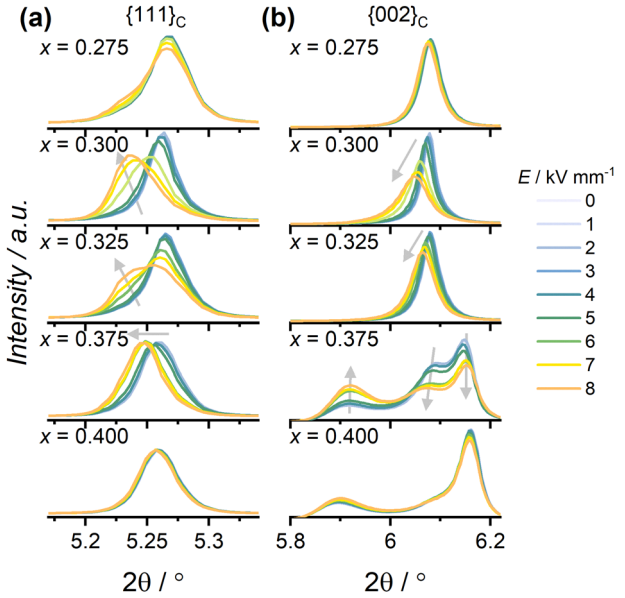

Fig. 2 X-ray diffraction patterns collected on BFTM–xPT (x = 0.275–0.400) at various applied electric fields where the $\{111\}_C$ and $\{002\}_C$ reflections are shown in (a) and (b), respectively. Data were collected at λ = 0.2116 Å, and ϕ = 0°.

parameters from the zero-field refinements are reported in Table S2, and the observed trends are consistent with those reported for polycrystalline samples in our previous work.[19]

The diffraction data collected parallel to the electric field (ϕ = 0°) on BFTM–xPT (x = 0.275–0.400) at various fields are shown in Fig. 2, highlighting the 2θ regions corresponding to the $\{111\}_C$ and $\{002\}_C$ reflections. The subscript "C" denotes the cubic structure and represents the family of peaks arising from all contributing phases (both PR and T reflections). Initial observations show that compositions x = 0.275 and 0.400 have little change in peak intensity and position, whereas compositions around the morphotropic phase boundary (MPB, x = 0.300–0.375) display larger changes with increasing field. Interestingly, the evolution of peak intensity and position does not follow the same trends for all compositions. Considering the $\{111\}_C$ family of reflections, shown in Fig. 2a, x = 0.300 and 0.325 display peak splitting, whereas x = 0.375 results in the shift of $\{111\}_C$ peak to lower 2θ. Furthermore, the $\{002\}_C$ reflections, shown in Fig. 2b, shift to the left and the peak shape broadens for x = 0.300 and 0.325. In contrast, for x = 0.375, there is a change in relative intensity of the $(002)_T$ and $(200)_T$ (at 5.92 and 6.15°, respectively), and the peak corresponding to the PR phase (at 6.07°) decreases in intensity upon application of the electric field. The differences in trends between compositions suggest that the mechanisms behind the piezoelectric response are not the same.

The diffraction data collected before poling, during poling (at 8 kV mm^{-1}) and after poling (at 0 kV mm^{-1}) are shown in Fig. S5. The data reveal that the structure does not revert back to the initial configuration after poling, indicating that poling of BFTM–xPT (x = 0.275–0.400) ceramics is an irreversible process. The presence of residual polarization after removal of the electric field is consistent with a ferroelectric material.

Upon application of an electric field to a ferroelectric ceramic, a portion of the domains reorient to align their internal polarization to a more preferred direction to the E-field. Given the polarization induces a preferred crystallographic direction, the domain reorientation introduces texture, or preferred orientation, in the diffraction pattern. By quantifying the texture that develops, the extent of domain alignment within individual crystallites can be inferred. The resulting field-induced texture manifests itself as changes of relatively intensities of diffraction peaks at a given 2θ along the ϕ-axis, and can be quantified by full-pattern-fitting through Rietveld refinement.[37]

Full-pattern Rietveld refinements of BFTM–xPT (x = 0.300–0.400) were completed, where strain, texture and scale factors of each phase were refined. The comparison of the experimental and calculated data are shown in Fig. 3, and a summary of the quality of fit (R_{wp}) is reported in Table S3.

Texture is reported in units of multiples of a random distribution (m.r.d.), where a value of 1 represents a randomly oriented material and the theoretical maxima of completely aligned domains are 3 and 4 for $[002]_T$ and $[111]_R$ (where R denotes the rhombohedral structure) directions, respectively.[38] The term f_{hkl} denotes the value of a hkl pole figure in a specific

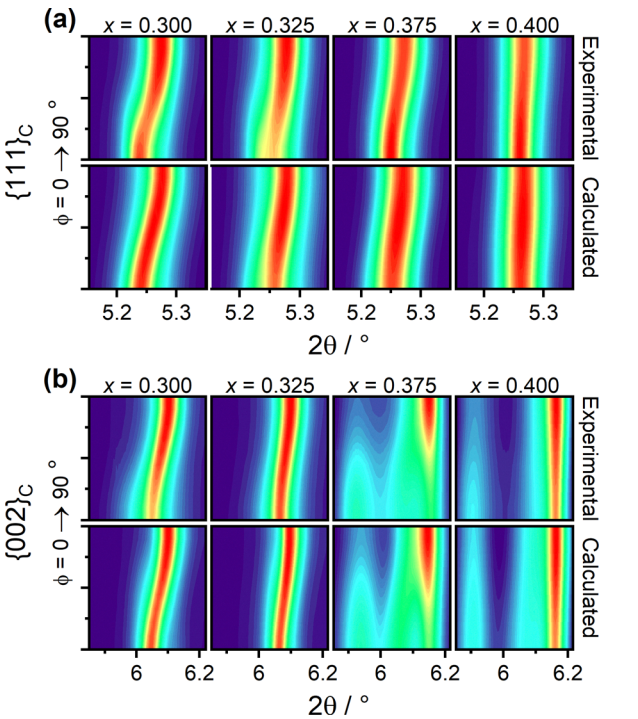

Fig. 3 Experimental and calculated intensities of diffraction data collected on BFTM–xPT (x = 0.300–0.400) at 8 kV mm^{-1} as a function of angle to electric field (ϕ), shown for the $\{111\}_C$ (a) and the $\{002\}_C$ (b) family of reflections. The experimental data are shown at the top of each panel, with corresponding calculated models below. The calculated data was obtained from texture refinements. The intensity values are plotted using the square root of intensity for ease of visualization.

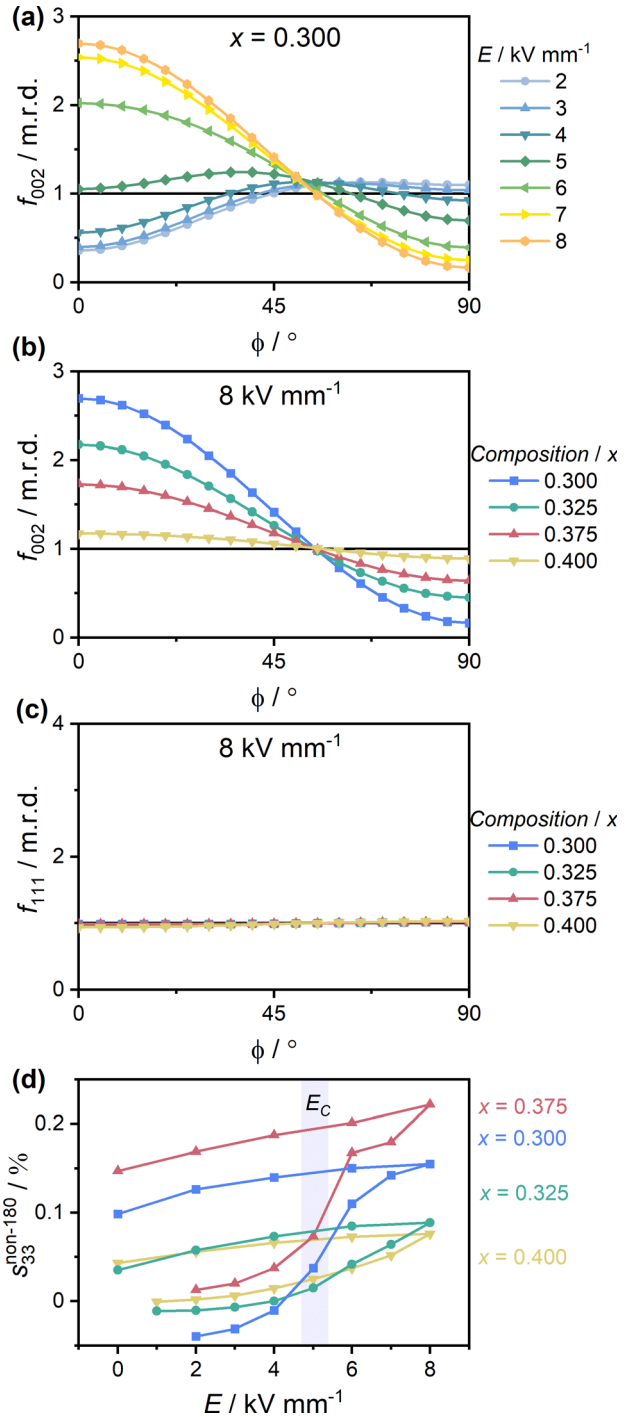

Fig. 4 Calculated f_{hkl} from Rietveld refinements. (a) 002_T pole figures under various applied electric fields. (b) Summary of 002_T pole figure at 8 kV mm^{-1} across BFTM–xPT compositions. (c) 111_R pole figures of BFTM–xPT (x = 0.300–400) at 8 kV mm^{-1}. The y-axes are drawn to represent the maximum theoretical f_{hkl} for each reflection (*i.e.* 3 m.r.d. for 002_T and 4 m.r.d. for 111_R). (d) The $s_{33}^{\text{non-180}}$ from tetragonal (T) phase (space group *P4mm*) domain wall motion in BFTM–xPT (x = 0.300–0.400). The shaded region signifies the coercive field (E_c) reported by Rowe *et al.*[15]

direction of the sample in units of m.r.d. The calculated texture within the T and PR phases of BFTM–xPT (x = 0.300–0.400) are shown in Fig. 4.

Fig. 4a shows the evolution of f_{002} of the T phase in composition x = 0.300 under an applied electric field. With increasing field, f_{002} aligned parallel to the field direction (ϕ = 0°) progressively increases, reaching a maximum value of 2.6 m.r.d. at 8 kV mm^{-1}. The onset of texture at 6 kV mm^{-1}, representing the alignment of dipoles with the electric field, occurs above the coercive field (E_c = 4.7 kV mm^{-1}).[15] The low-field non-zero f_{002} values are attributed to geometry-dependent profile broadening inherent to bar-shaped transmission samples, which produce a wider distribution of X-ray path lengths that result in ϕ-dependent scattering and peak broadening in the ϕ = 90° sector.[39] The complete sets of calculated f_{hkl} at each field and composition are provided in Fig. S6 and S7.

Fig. 4b and c compare the f_{002} of the T phases and the f_{111} of the PR phases at 8 kV mm^{-1} for all compositions. Within the T phases (Fig. 4b), x = 0.300 exhibits the highest degree of domain alignment, with a f_{002} of 2.6 m.r.d. parallel to the E-field (ϕ = 0°). Compositions x = 0.325 and 0.375 also show significant alignment, with maximum f_{002} values of 2.1 and 1.8 m.r.d., respectively. In contrast, the PR phases in all compositions do not exhibit measurable texture ($f_{111} \approx 1$, see Fig. 4c), indicating the absence of domain wall motion in the PR phase.

The contribution of strain induced by non-180° domain wall motion of the T phase was calculated using eqn (3).[38]

$$s_{33}^{\text{non-180}} = \frac{c-a}{a}\frac{1}{2\pi}\int_{\phi=0}^{\pi/2} \Delta f_{hkl^*}(\phi)\cdot\cos^2\phi\cdot\sin\phi \mathrm{d}\phi \qquad (3)$$

The term Δf_{hkl^*} represents the change in pole figure direction $\left(f_{hkl_E^*} - f_{hkl_0^*}\right)$, ϕ denotes the angle between the applied E-field and the scattering vector, and the $(c-a)/a$ term accounts for the T lattice distortion, with a and c being the lattice parameters, reported in Table S2.

The $s_{33}^{\text{non-180}}$ arising from the T domain wall motion as a function of applied field are shown in Fig. 4d. The composition x = 0.375 exhibits the highest maximum strain. Although the MPB compositions (x = 0.300 and x = 0.325) show greater domain wall motion (f_{002}) than x = 0.375, they have much smaller lattice distortions $(c-a)/a$ (0.0101 and 0.0093, respectively) compared to x = 0.375 (0.0354). Consequently, the MPB compositions generate smaller T domain wall motion strain. In contrast, the larger unit cell distortion in x = 0.375 leads to the highest strain due to T domain wall motion despite its lower f_{002}. Meanwhile, x = 0.325 contributes only minimally to the macroscopic strain because it has the smallest lattice distortion.

It is noted that when the PR phase is modeled by space group *Cc*, evidence of texture along the $[111]_C$ direction is observed for compositions x = 0.300 and 0.325, with maximum values of 3.2 and 1.9 m.r.d., respectively, as shown in Fig. S3. Despite the relatively strong textures, the corresponding strain contribution is less than 0.03% (Fig. S4) due to the small lattice distortion. The small $s_{33}^{\text{non-180}}$ from the PR phase suggests that while domain walls of the PR phase (in x = 0.300 and 0.325 compositions) may exhibit high mobility, their contribution to

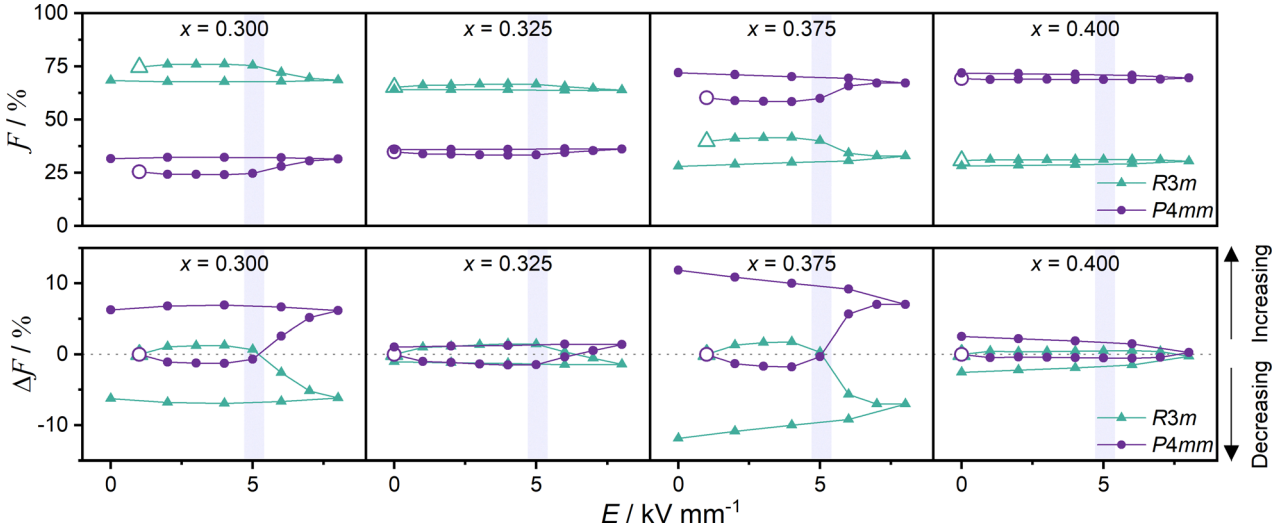

Fig. 5 Evolution of phase fractions in BFTM–*x*PT (x = 0.300–0.400) upon applied electric field. Top panels show the absolute phase fractions ($\mathcal{F}$) of the *R3m* and *P4mm* phases, while the bottom panels show the change in phase fractions ($\Delta\mathcal{F}$, see eqn (4)). Phase fractions were obtained from the refined scale parameters during Rietveld refinements of diffraction data collected from 0–8 kV mm^{-1} in 1-kV mm^{-1} steps during field application, and in −2-kV mm^{-1} steps during field removal. The first measurement of each dataset is indicated by the large open symbol. Shaded regions at ∼5 kV mm^{-1} highlight the coercive field (E_c) reported by Rowe *et al.*[15]

the macroscopic strain remains negligible. Overall, regardless of the choice of space group to describe the unit cell, the domain wall motion in the PR phase contributes minimally to the total strain, suggesting the presence of an additional mechanism that is explored in more detail in Section 3.2.

Diffraction data also provide quantitative insight into the phase fractions within the ceramic. The evolution of phase fractions ($\mathcal{F}$) within each composition is shown in Fig. 5a. A clear compositional trend is observed: the fraction of the PR phase (space group *R3m*) decreases progressively as the amount of $PbTiO_3$ (x) increases. Among BFTM–*x*PT, compositions x = 0.300 and 0.375 exhibit the most pronounced field-induced changes in phase fraction. To highlight variations in $\mathcal{F}$, the change in phase fraction ($\Delta\mathcal{F}$, defined in eqn (4)) is plotted as a function of applied E-field in the bottom panel of Fig. 5.

$$\Delta\mathcal{F} = (\mathcal{F}_E - \mathcal{F}_0) \cdot 100\% \quad (4)$$

The term $\mathcal{F}_E$ represents the phase fraction at a given applied field, and $\mathcal{F}_0$ corresponds to the initial phase fraction of the sample. A positive change ($\Delta\mathcal{F} > 0$) indicates an increase in the fraction of that phase, while a negative value ($\Delta\mathcal{F} < 0$) corresponds to a decrease. All investigated compositions (x = 0.300–0.400) exhibit a field-induced pseudorhombohedral-to-tetragonal (PR-to-T) phase transition, as evidenced by an increase in $\Delta\mathcal{F}$ of the T phase ($\Delta\mathcal{F}_T$) with applied electric field. The $+\Delta\mathcal{F}_T$ reflects interphase boundary motion, in which the interface between PR and T crystallographic phases moves such that the T phase is favoured and grows in population. The largest absolute increase in $\mathcal{F}_T$ (8.2%) is in composition x = 0.375. Notably, in x = 0.375 composition, the increase in $\mathcal{F}_T$ continues as the field is removed, reaching a final $\Delta\mathcal{F}_T$ of +14.9%. A similar, though less pronounced, trend also is observed for x = 0.400 where $\mathcal{F}_T$ increases by +2.5%. In contrast, the PR dominant compositions also exhibit a *R3m* to *P4mm* phase transition, but unlike x = 0.375, increase in $\Delta\mathcal{F}_T$ does not persist once the field is removed. The greatest change is seen in the composition x = 0.300, which has a $\mathcal{F}_T$ increase of +6.3%, while the composition x = 0.325 has a near-negligible increase in $\mathcal{F}_T$ upon poling (≈1%).

The diffraction data reveal that extrinsic mechanisms, including domain wall motion and interphase boundary motion (increase in the T phase) contribute to the piezoelectric response of the x = 0.375 composition. In contrast, even though x = 0.325 has good piezoelectric performance as demonstrated by its macroscopic properties (d^*_{33} = 190 pm V^{-1} and strain = 0.19%),[15] extrinsic domain wall motion contributes minimally to the strain and interphase boundary motion is negligible. The absence of extrinsic contributions in the MPB composition suggests that intrinsic mechanisms may play an important role in governing its piezoelectric response.

3.2 Pair distribution function analysis

The pair distribution function was used to elucidate the subtle local structural changes induced by the applied electric field. For each composition, the PDF data collected before poling ($G(r)_0$), at the maximum applied field ($G(r)_{max}$), and their difference ($\Delta G(r)$) are compared in Fig. 6. The greatest changes are found in the compositions clustered around the MPB (x = 0.325–0.350), meaning that the applied field induces structural changes on the local scale. Thus, compositions x = 0.325–0.350 have an intrinsic contribution to their electromechanical properties. In contrast, the local structures of the compositions outside the MPB (x = 0.275–0.300 and 0.375–0.400) are less affected by an applied field, as seen by the suppressed $\Delta G(r)$.

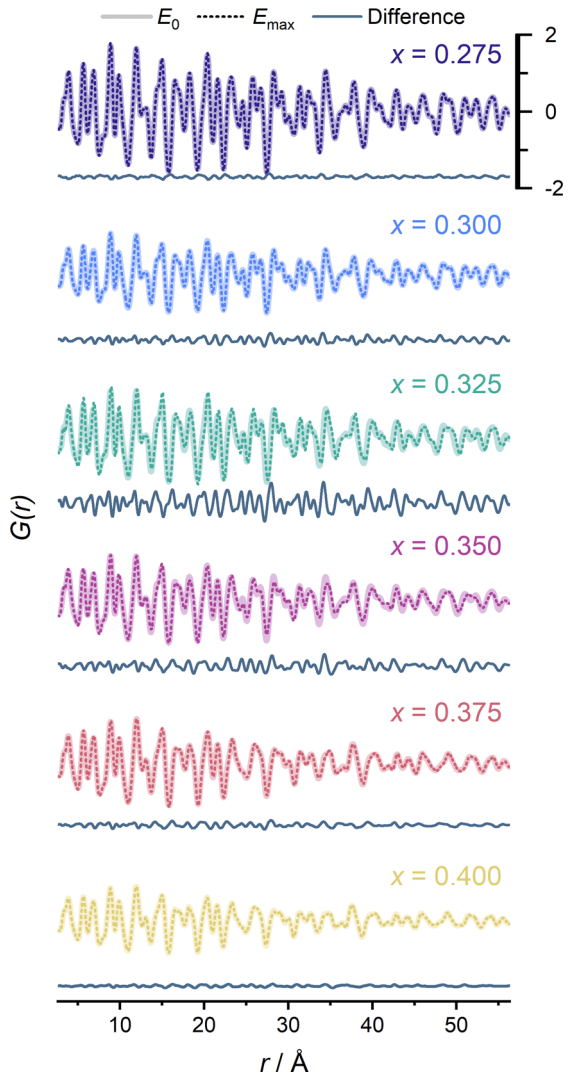

Fig. 6 Comparison of $G(r)$ parallel to the applied field (ϕ = 0°) for BFTM–xPT (x = 0.275–0.400) measured before (E_0 = 0 kV mm^{-1}) and during poling at the maximum applied field (E_{max} = 8 kV mm^{-1} for x = 0.300, 0.325, 0.375, and 0.400; 7 kV mm^{-1} for x = 0.275; and 6 kV mm^{-1} for x = 0.350).

The composition x = 0.325 has the highest magnitude of $\Delta G(r)$, demonstrating that significant structural changes occur on the local scale. Looking closer at how the local structure evolves with increasing electric field, Fig. 7 displays $G(r)$ on the short- and medium-length scales and compares two compositions: x = 0.325 (inside the MPB) and 0.375 (outside the MPB). The peak at 3.5 ± 0.3 Å corresponds to the A–B distances, and the peak at 4 Å corresponds to the A–A distances. The 20–30 Å region represents medium-range correlations that are approximately 5–8 unit cells apart. In composition x = 0.325, $G(r)$ changes with the electric field on both the short- and medium-length scales, where the peak at $r \approx$ 3.5 Å shifts to lower r and a systematic shift of the data to higher r occurs at medium-length scales. In contrast, there is minimal change outside the MPB for x = 0.375, as shown in Fig. 7.

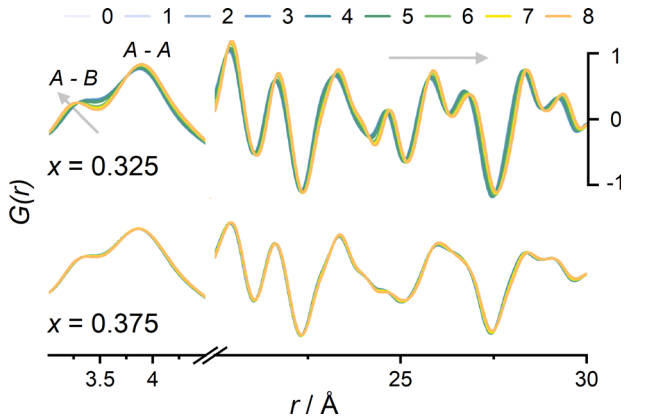

Fig. 7 Evolution of $G(r)$ (ϕ = 0°) for x = 0.325 (top) and x = 0.375 (bottom) upon application of a 8-kV mm^{-1} E-field. The low-r region (r = 3.0–4.5 Å) shows the features that correspond to the A-site (Pb^{2+} or Bi^{3+}) to B-site (Fe^{3+}, Ti^{4+} or Mg^{2+}) cation distances (A–B) and the A-site to A-site cation distances (A–A). The data collected on x = 0.325 show a peak shift to smaller r for the A–B features, whereas the high-r data shift to higher r-values upon application of a field. Trends are indicated by grey arrows. Conversely, the PDF data collected for x = 0.375 shows minimal change upon application of a field.

As the data in Fig. 7 were collected parallel to the applied electric field (ϕ = 0°), a shifting data to higher r indicates that the atom–atom correlations have lengthened, and an elongation of the unit cell in the direction that is parallel to the field has occurred. The systematic shift of peaks to higher r is a signature of piezoelectric lattice strain, and the remainder of this section will focus on understanding and quantifying piezoelectric lattice strain further.

Fig. 8 shows the residual shift, δr (defined in eqn (2)), for x = 0.275–0.400 compositions. A larger magnitude of δr corresponds to a larger shift between $G(r)_0$ and $G(r)_E$. The highest δr values are found in the compositions around the MPB (x = 0.300–0.350), with the maximum δr values found in composition x = 0.325.

For x = 0.300–0.350, δr increases in magnitude with: (1) increasing r (interatomic distance); and (2) increasing electric

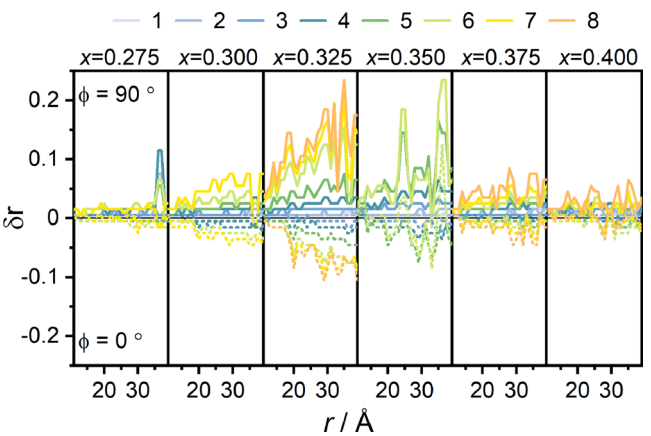

Fig. 8 PDF peak shifts (δ_r) parallel (ϕ = 0°) and perpendicular (ϕ = 90°) to the field across r for electric fields ranging from 1–8 kV mm^{-1}.

field strength. Crystal poles aligned parallel to the electric field exhibit a positive shift, corresponding to unit cell elongation along the field direction, whereas crystal poles oriented perpendicular to the field exhibit a negative shift, indicating contraction perpendicular to the field. The magnitude of δr parallel to the field is larger than the δr perpendicular to it, reflecting the anisotropic nature of the field-induced strain. Similar anisotropic lattice strain have also been observed in $(1-x)Ba(Zr_{0.2}Ti_{0.8})O_3$–$x(Ba_{0.7}Ca_{0.3})TiO_3$ and $(K_xNa_{1-x})_{0.5}Bi_{0.5}TiO_3$ ceramics.[23,26]

The δr gradient represents the local strain in the material and provides insight into the mesoscale piezoelectric coefficients.[35] Fig. 9 compares the mesoscale strain of BFTM–xPT (x = 0.300–0.375) with that of other ferroelectric materials. The maximum strain was observed for the MPB composition (x = 0.325) with a value of 4.5×10^{-3}, indicating that the MPB composition exhibits the largest intrinsic response to an applied E-field relative to compositions outside of the MPB.

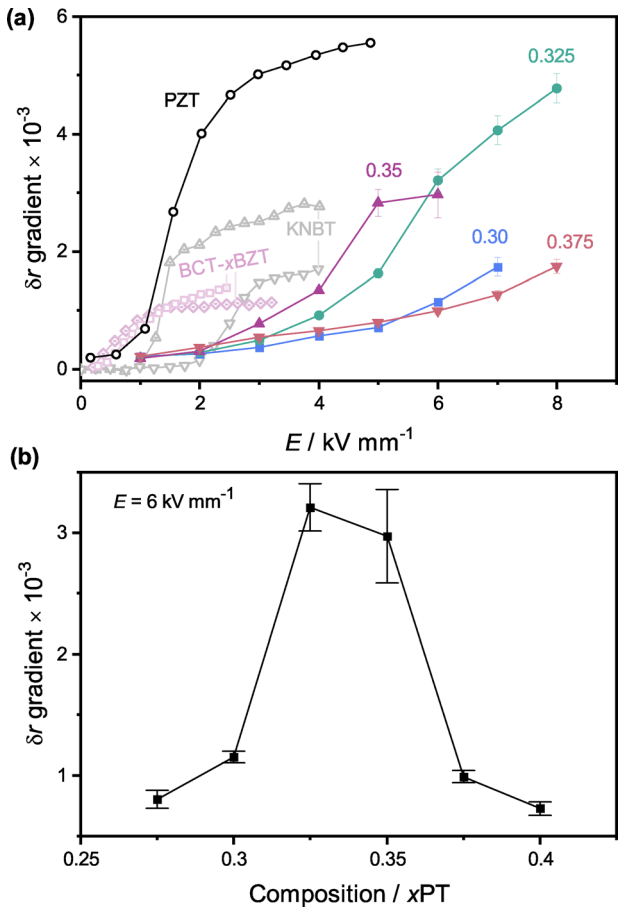

Fig. 9 Intrinsic strain (δ_r gradient) of BFTM–xPT (x = 0.300–0.375) compared to common literature materials. BFTM–xPT are represented by closed circles: x = 0.300 (—■—), x = 0.325 (—●—); x = 0.35 (—▲—), and x = 0.375 (—▼—). Literature references include: $PbZr_{0.54}Ti_{0.56}O_3$ (—○—),[25] $(K_{0.20}Na_{0.8})_{0.5}Bi_{0.5}TiO_3$ (—▽—),[23] $(K_{0.15}Na_{0.85})_{0.5}Bi_{0.5}TiO_3$ (—△—),[23] $(1-x)Ba(Zr_{0.2}Ti_{0.8})O_3$–$x(Ba_{0.7}Ca_{0.3})TiO_3$ for x = 0.45(—◇—) and x = 0.55 (—□—).[26] (b) Comparison of the δ_r gradient as a function of composition of BFTM–xPT (x = 0.300–0.375) at a maximum applied field (E) of 6 kV mm^{-1}.

Compared to other ferroelectric materials, the MPB composition, x = 0.325, exhibits an intrinsic strain similar to the industry-standard piezoelectric material $PbZr_{0.54}Ti_{0.46}O_3$, whereas x = 0.300, 0.350, and 0.375 show magnitudes similar to those reported for $(1-x)Ba(Zr_{0.2}Ti_{0.8})O_3$–$x(Ba_{0.7}Ca_{0.3})TiO_3$ and $(K_xNa_{1-x})_{0.5}Bi_{0.5}TiO_3$ ceramics.[23,26]

For x = 0.300–0.350, there are two regions in the δr gradient: (i) below approx. 5 kV mm^{-1}, where δr gradient increases gradually; and (ii) above approx. 5 kV mm^{-1}, where the slope of δr gradient becomes steeper. The onset of region (ii) coincides with the coercive field[15] and with an increase of f_{002} indicating the initiation of domain wall motion. The simultaneous increase of δr gradient and f_{002} (see Fig. S6) near 5 kV mm^{-1} suggests that the lattice strain is intricately tied with domain wall motion.

The high-field linear region of the δ_r gradient was linearly fit (see Fig. S9) and the slope was obtained, which represents the intrinsic contribution to the high-field piezoelectric coefficient (d_{33}^*), referred to as the intrinsic d_{33}^*, corresponding to piezoelectric lattice strain. The intrinsic d_{33}^* values are reported in Fig. 10 and are compared to the d_{33}^* originating from domain wall motion (details for calculating the extrinsic d_{33}^* are included in the SI, see eqn (S1)–(S3)). The piezoelectric lattice strain is maximized at x = 0.325, and decreases as the composition moves further away from the MPB. In contrast, the extrinsic strain, originating from T domain wall motion, is highest at x = 0.375.

The bulk d_{33}^* and bulk d_{33} data previously reported by Rowe *et al.*[15] are included in Fig. 10 to directly compare the d_{33}^* calculated from the total scattering experiments to the bulk d_{33}^* measured from the ceramic. Differences in poling history between bulk and total scattering experiments may introduce

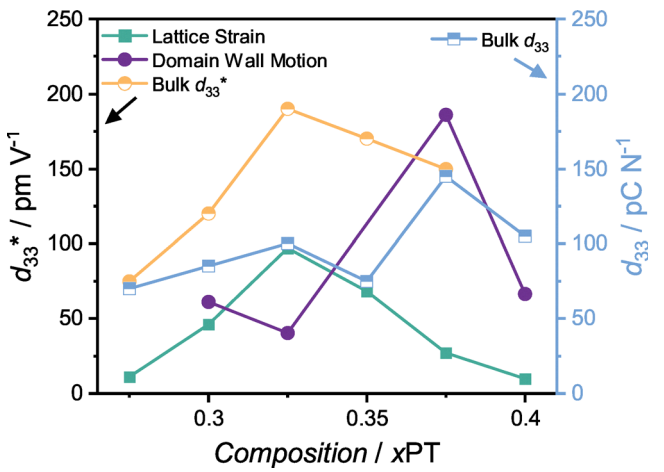

Fig. 10 Comparison of the high-field piezoelectric coefficient (d_{33}^*) originating from extrinsic domain wall motion and intrinsic piezoelectric lattice strain. The extrinsic d_{33}^* was calculated from the $s_{33}^{non\text{-}180}$, while the intrinsic strain is calculated from δr gradient. Further details of these calculations are reported in the SI (S5). The bulk d_{33}^* and bulk d_{33} data previously reported by Rowe *et al.*[15] plotted to compare the d_{33}^* calculated from the total scattering experiments to the bulk d_{33}^* measured directly from the ceramic.

minor variations in piezoelectric coefficients; however, the compositional trends remain consistent. The maximum lattice strain coincides with the maximum bulk d_{33}^* at x = 0.325, whereas the maxima in domain wall motion and d_{33} both occur at x = 0.375. The correlation between lattice strain and the bulk d_{33}^* demonstrates that intrinsic lattice strain dominant the high-field electromechanical response within the MPB. In contrast, the correlation between domain wall motion and bulk d_{33} indicates that the extrinsic domain wall contributions govern the low-field electromechanical response outside the MPB. Overall, the comparison of intrinsic and extrinsic d_{33}^* values indicates that the intrinsic strain is maximized at x = 0.325, while the extrinsic strain is maximized at x = 0.375.

4 Discussion

This article investigated the average and local structural changes in BFTM–xPT under an applied electric field. The most significant field-induced changes were observed for compositions at and near the MPB (x = 0.300–0.375), as visible in the diffraction (Fig. 2) and PDF (Fig. 6) data. By contrast, compositions further from the MPB exhibit only minimal structural responses. For the rhombohedral composition (x = 0.275), the limited response is likely due to its pronounced degree of octahedral tilting.[19] Octahedral tilting induces an antiferrodistortion that effectively clamps domain walls and suppresses extrinsic contributions;[40] octahedral tilting has been shown to decrease piezoelectric performance.[20]

On the T side of the MPB, the x = 0.400 composition also displays modest structural changes in both diffraction and PDF data (Fig. 2 and 6), potentially due to the increased tetragonality of the unit cell. As the concentration of $PbTiO_3$ (x) increases, tetragonality increases while the domain wall mobility correspondingly decreases. For x = 0.400, f_{002} is 1.2 m.r.d. and c/a ratio is 1.043, whereas for x = 0.375, f_{002} increases to 1.7 m.r.d. and exhibits a lower c/a ratio of 1.035. The inverse correlation between unit cell distortion and domain wall mobility is similar to the trend observed in $(1-x)Ba(Zr_{0.2}Ti_{0.8}O_3)$–$x(Ba_{0.7}Ca_{0.3})TiO_3$, where compositions with lower tetragonality (closer to the MPB) exhibit greater domain wall motion.[26,41]

Compositions within the MPB (x = 0.300 and 0.325) exhibit the highest domain wall motion in the T phase (f_{002}), as shown in Fig. 4b, meaning that domains more easily align with the external E-field which consistent with Martensitic-based theory that states that the domain wall motion is enhanced at the MPB.[42] The enhanced domain reorientation in the MPB is also present in $(1-x)Ba(Zr_{0.2}Ti_{0.8}O_3)$–$x(Ba_{0.7}Ca_{0.3})TiO_3$,[26] $(K_xNa_{1-x})_{0.5}Bi_{0.5}TiO_3$,[23] and Nb-doped PZT.[25] However, the enhanced domain wall motion within the MBP is in contrast to the compositionally and structurally similar system $BiScO_3$–$PbTiO_3$ (BS–PT), where BS–PT does not support the Martensitic model and exhibits decreased domain wall motion in the MPB. Instead, the high piezoelectric performance of BS–PT arises from an electric-field-driven phase transition.[43] The contrast between Martensitic-driven behaviour in BFTM–xPT and the field-induced phase transitions in BS–PT highlights the diversity of mechanisms within the $BiMO_3$–$PbTiO_3$ family of materials, despite structural and chemical similarities.

In comparison to other tsystems, the T domain wall motion within the composition x = 0.375 (f_{002} = 1.8 m.r.d.) is slighter larger in magnitude compared to $BiMg_{0.5}Ti_{0.5}O_3$–$PbTiO_3$ (f_{002} = 1.7 m.r.d. at E = 4.8 kV mm^{-1})[44] and $BiNi_{0.5}Ti_{0.5}O_3$–$PbTiO_3$ (f_{002} = 1.4 m.r.d. at E = 5.2 kV mm^{-1}).[45] Alternatively, the MPB compositions of x = 0.300 and 0.325 exhibit a larger magnitude of domain wall motion with f_{002} = 2.6 m.r.d. and 2.1 m.r.d. at E = 8 kV mm^{-1}, respectively. These values closely match the magnitude of domain wall motion seen in non-MPB $0.35BiNi_{0.5}Hf_{0.5}O_3$–$0.65PbTiO_3$ (f_{002} = 2.2 m.r.d. at E = 5 kV mm^{-1}),[46] and modified $BiFeO_3$–$PbTiO_3$ ($0.6Bi_{0.95}La_{0.05}FeO_3$–$0.2PbTiO_3$–$0.2BaTiO_3$, f_{002} = 2.2 m.r.d. at E = 6 kV mm^{-1}).[47]

No PR domain wall motion is observed throughout the series of compositions studied (Fig. 4c). Interpretation of the PR phase is, however, limited by the model. In this present work, the PR phase was modeled by space group $R3m$, although our previous study showed it is more accurately characterized by monoclinic space groups Cc (for x = 0.275–0.35) and Cm (for x = 0.375).[19] As a result, potential domain wall motion within the monoclinic structures (Cc and Cm) may be present but is beyond the resolution limits of our dataset. Refinements against x = 0.300 and 0.325 using the $P4mm$ + Cc model reveals evidence of possible domain wall motion, but confidence is low due to highly correlated parameters and significant peak overlap. Accordingly, results are reported using the approximated $R3m$ model, while noting that future studies are necessary to investigate potential domain wall motion in the monoclinic structures. Piezoresponse force microscopy (PFM) or transmission electron microscopy (TEM) are promising potential experiments that aid in understanding domain structures and domain density.

Although the highest T domain wall motion is observed within the MPB, the relatively low T phase fraction and the small unit cell distortion (c/a = 1.01, see Table S2 for lattice parameters obtained from refinements) mean that the domain wall motion contributes only a minor fraction of the total strain (extrinsic $d_{33}^* = 40$ pm V^{-1}). Instead, the large strain is primarily achieved through an intrinsic mechanism, as evidenced by the PDF analysis (intrinsic $d_{33}^* = 97$ pm V^{-1}). The relative contributions of intrinsic and extrinsic d_{33}^* to the total electrostrain in x = 0.325 stand in stark contrast to those in x = 0.375, where the extrinsic d_{33}^* is 186 pm V^{-1} and the intrinsic contribution is only 27 pm V^{-1} (as shown in Fig. 10), highlighting how compositional tuning can fundamentally alter the balance of intrinsic and extrinsic mechanisms. Notably, the average grain size is similar ($\sim$1 μm) across the BFTM–xPT solid solution (Fig. S1) demonstrating that the mechanistic differences originate from differences in chemistry rather than changes in the microstructure.

The large contribution of intrinsic strain within the MPB is also present in other perovskite ferroelectric systems including $(K_xNa_{1-x})_{0.5}Bi_{0.5}TiO_3$,[23] Nb-doped PZT,[25] and $(0.75-x)BiFeO_3$–$PbTiO_3$–$xBa(Zr_{0.25}Ti_{0.75})O_3$,[48] but interestingly this feature is

not present in compositionally similar BS–PT.[43] The difference in mechanisms between BS–PT and BFTM–xPT shows that enhanced intrinsic strain within the MPB is not a universal feature and it is important to investigate each system individually to fully understand the electromechanical mechanism.

With increasing electric field, composition $x = 0.375$ exhibits growth in the T phase fraction at the expense of the PR phase, indicating interphase boundary motion (as displayed in Fig. 5). During interphase boundary motion, the PR regions undergo a phase transition to the T structure, thereby shifting the phase boundary and increasing the overall T phase fraction. A schematic of mechanisms in composition $x = 0.375$ are drawn in Scheme 2a, where the domains aligned with the E-field grow in size resulting in: (1) the domains not aligned with field to decrease; and (2) phase transformation of the PR unit cells along the grain boundary to transition to T, consequently moving the interphase boundary and increasing the T phase fraction. Similar PR-to-T phase transitions occur in BS–PT,[43] $BiMg_{0.5}Ti_{0.5}O_3$–$PbTiO_3$,[44] and $0.93Bi_{0.5}Na_{0.5}TiO_3$–$0.07BaTiO_3$.[49] In contrast, modified-PZT[50] and $BiNi_{0.5}Hf_{0.5}O_3$–$PbTiO_3$[46] undergo interphase boundary motion that favours a monoclinic phase, accompanied by a tetragonal-to-monoclinic phase transition.

Unlike $x = 0.375$, the phase fractions of the MPB composition, $x = 0.325$, remain essentially unchanged upon poling (see Fig. 5), indicating that interphase boundary motion does not contribute to piezoelectric performance within the MPB. Despite the lack of change in the average structure, the PDF data (Fig. 7) reveal pronounced structural changes on the local- and medium-length scales, suggesting that the short- and medium-range structural distortions in $x = 0.325$ do not propagate with sufficient long-range coherence to modify the description of the average crystallographic structure. As a result, the refined average structure and the associated phase fractions remain unchanged even though substantial local distortions occur.

A prominent feature in the PDF data (Fig. 7) is the apparent shift of the A–B bond length ($r \approx 3.5$ Å) to low-r which is attributed to domain switching that redistributes local A–B bond directions rather than contracting the bond distance as a shift to lower r might suggest. Evidence of bond redistribution has also been reported in $Na_{0.5}Bi_{0.5}TiO_3$ where the PDF data similarly exhibited a low-r peak shift near $r \approx 3.5$ Å,[22] consistent with the behaviour observed in BFTM–xPT ($x = 0.325$).

In addition, the PDF data also reveals a systematic shift of peaks to high-r which can be used to extrapolate the intrinsic strain which is plotted in Fig. 9. The intrinsic strain exhibits a strong correlation with domain wall motion, as it emerges at the same voltage where the field-induced texture develops. A likely driving force for intrinsic strain is intergranular elastic interactions induced by accumulative stress in neighbouring grains undergoing significant non-180° domain switching.[51] Intergranular stress is depicted in Scheme 2b, where the domain alignment with the electric field results in the lengthening of the grain ($+\Delta L$) which consequently strains neighbouring grains. The intergranular strain caused domain wall motion interpretation is further supported by the irreversibility of both the domain wall motion and intrinsic strain, as demonstrated in the comparison of diffraction and PDF data collected before and after poling (shown in Fig. S5 and S8). The observed trends are consistent with Nb-doped PZT, where domain wall motion and strain are intricately related.[25] In both Nb-doped PZT and BS–PT, remanent strain originates from domain wall motion, and this also appears to be the case in BFTM–xPT.

A more comprehensive understanding of the local structural distortions in the MPB of BFTM–xPT would require additional experimental approaches. A key limitation of the X-ray PDF measurements is their insufficient sensitivity to resolve the B–O and A–O correlations, which limits a detailed assessment of local rearrangements. This limitation precludes the use of boxcar modeling to extract the specific bond lengths and displacement directions. Neutron scattering is one potential alternative for probing these correlations, although it presents practical challenges: time-of-flight beamlines require complex data reduction procedures,[52] while reactor-based beamlines often lack the flux necessary for high-quality PDF measurements.

Recent work by Yao *et al.* demonstrated that reverse Monte Carlo (RMC) modeling of neutron PDF data can be used to effectively describe both the local atomic distortions and the distribution of polarization orientations in ferroelectric ceramics.[53] Yao *et al.* further highlighted that piezoelectric performance is governed not only by the magnitude of polarization, but also by orientational disorder arising from local

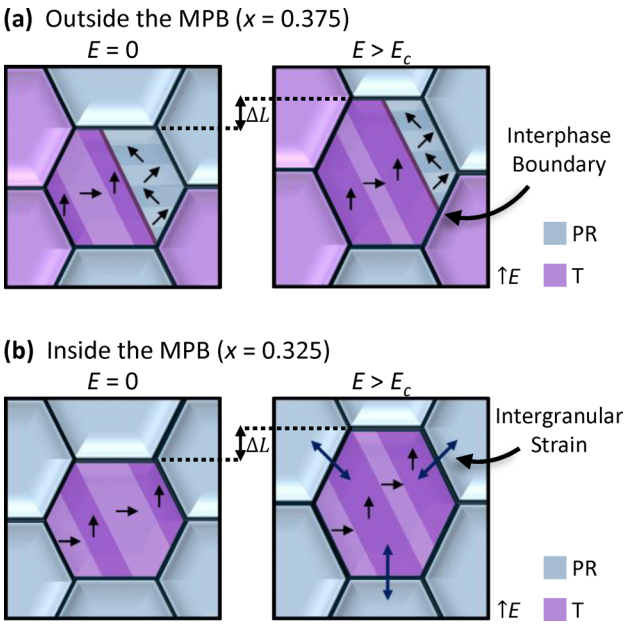

Scheme 2 Visual representation of potential piezoelectric mechanisms in BFTM–xPT resulting in the elongation of grains in the same direction as E-field ($+\Delta L$). (a) Outside the MPB, piezoelectric response arises from both domain wall motion and interphase boundary motion. (b) Inside the MPB, tetragonal (T) domain wall motion induces intergranular strain to neighbouring pseudorhombohedral (PR) grains. Purple domains denote T regions and grey domains denote PR regions.

dipole fluctuations.[53] Notably, the materials studied by Yao *et al.* were compositionally simpler than BFTM–*x*PT. Neutron PDF measurements on $BiFe_{2/8}Ti_{3/8}Mg_{3/8}O_3$ have already proven challenging to analyze due to the large the large number of pair correlations.[54] Therefore, the addition of further A-site substitution in BFTM–*x*PT, along with the application of an electric field, would significantly increase the complexity of both data collection and modeling. Nevertheless, the dominance of a low-symmetry PR phase within the MPB gives the polarization vector increased orientational freedom, which may promote dipole disorder. Such disorder could explain why local changes are not visible in the average structure. Thus, RMC modeling of neutron PDF data for BFTM–*x*PT, while experimentally and computationally demanding, could clarify how local distortions and polarization disorder combine to influence electromechanical behaviour.

Importantly, neutron PDF would also provide a direct means to investigate a key unresolved questions in this work, namely the pronounced disparity between the low- and high-field piezoelectric coefficients within the MPB compositions (x = 0.300–0.350), as shown in Fig. 1. One hypothesis for the much higher d^*_{33} is the occurrence of a reversible high-field local structural phase transition that generates additional local distortions which enhances the high-field response, but is reversed upon field removal, thereby not contributing to the low-field d_{33}. Because this proposed transition is expected to be short-ranged, it would not be visible in the average structure diffraction; however, *in situ* neutron PDF would be well suited to capture the subtle, field-induced rearrangements of the oxygen octahedra and cation displacements associated with a local phase transition. Although neutron PDF measurements lie beyond the scope of the present study, our results provide an essential foundation and motivation for more intricate investigations of the local structure of BFTM–*x*PT to resolve this outstanding question.

Elucidating the origin behind piezoelectric response provides an explanation for the substantial composition-dependent variations in the bulk macroscopic piezoelectric coefficients reported in our previous work (Fig. 1).[15] For x = 0.375, extrinsic contributions dominate the electromechanical response with a PR-to-T phase transition and extensive domain wall motion. The phase transition is non-reversible explaining the large d_{33} of 145 pC N^{-1} upon removal of the field. In contrast, the MPB composition (x = 0.325) displays a lower d_{33} of 100 pC N^{-1}, but a high d^*_{33} of 190 pm V^{-1}. The present findings indicate that intrinsic lattice strain is the dominant contributor to its electromechanical response at high fields. Thus, the compositional variations in the bulk macroscopic properties can be attributed to fundamental differences in the electrostrain mechanisms.

This study has focused on the high-field piezoelectric response d^*_{33}, demonstrating that intrinsic mechanisms dominate in the MPB, whereas extrinsic mechanisms govern the T-rich region (x = 0.375). Future neutron PDF studies would provide an essential path forward, for resolving the local structural distortions underlying these mechanisms and for determining whether a reversible high-field local structural transition is responsible for the observed divergence between low- and high-field piezoelectric coefficients in the MPB.

5 Conclusions

This work studied the average and local structure of BFTM–*x*PT under applied electric field using *in situ* electric field total scattering. This investigation revealed that compositions at (or near) the MPB have the largest structural response to the external electric field, and that the mechanism is dependent on the concentration of $PbTiO_3$. Outside the MPB, in the T-rich region (at x = 0.375), strain originating from extrinsic contributions are dominant. In composition x = 0.375, 86% of the total strain originates from T domain wall motion. In addition, interphase boundary motion is also present as x = 0.375 undergoes a 14.9% PR-to-T phase transition. Conversely, strain originating from intrinsic effects dominate the piezoelectric response inside the MPB (at x = 0.325). Within the MPB, no phase transition occurs. Instead, 71% of the piezoelectric response originates from piezoelectric lattice strain caused by intergranular stress from non-180° domain reorientation occurring in the minor T phase. The ceramic BFTM–*x*PT provides an example of a solid solution with a high-performance composition beyond the conventional MPB regime, demonstrating that useful ferroelectrics can also exist outside the MPB. Furthermore, this article illustrates how the electrostrain mechanisms can be controlled through composition. Mechanistic control *via* compositional tuning offers a powerful strategy for designing materials optimized for targeted applications.

Conflicts of interest

There are no conflicts to declare.

Data availability

The data supporting this article have been included as part of the supplementary information (SI). Supplementary information: Tables S1–S3, Fig. S1–S9, further experimental details and calculations. See DOI: https://doi.org/10.1039/d6tc00067c.

Acknowledgements

This research was performed on APS beam time award (DOI: https://doi.org/10.46936/APS-180673/60009880) from the Advanced Photon Source, a U.S. Department of Energy (DOE) Office of Science user facility operated for the DOE Office of Science by Argonne National Laboratory under Contract No. DE-AC02-06CH11357. The authors gratefully acknowledge the support and guidance Dr Olaf J. Borkiewicz and Dr Leighanne Gallington during the beamline experiment. They also thank the Natural Sciences and Engineering Research Council (NSERC), Alberta Innovates, and Killam Research funds for this research. Additionally, the authors express their appreciation to

the University of Calgary, the Canadian Foundation for Innovation (John R. Evans Leaders Fund) and the Canada First Research Fund (CFREF) for funding the facilities used in this study. They thank C. DeBuhr for assistance with SEM sample preparation and image acquisition. Furthermore, the University of Calgary, located in the heart of Southern Alberta, both acknowledges and pays tribute to the traditional territories of the peoples of Treaty 7, which include the Blackfoot Confederacy (comprised of the Siksika, the Piikani, and the Kainai First Nations), the Tsuut'ina First Nation, and the Stoney Nakoda (including Chiniki, Bearspaw, and Goodstoney First Nations). The City of Calgary is also home to the Métis Nation of Alberta (Districts 5 and 6).

Notes and references

1 A. M. Manjón-Sanz and M. R. Dolgos, *Chem. Mater.*, 2018, **30**, 8718–8726.
2 R. Turner, P. Fuierer, R. Newnham and T. Shrout, *Appl. Acoust.*, 1994, **41**, 299–324.
3 G. W. Hunter, J. D. Wrbanek, R. S. Okojie, P. G. Neudeck, G. C. Fralick, L. Chen, J. Xu and G. M. Beheim, *Sensors for Propulsion Measurement Applications*, 2006, p. 622209.
4 L. Yule, B. Zaghari, N. Harris and M. Hill, *Meas. Sci. Technol.*, 2021, **32**, 052002.
5 S. Zhang and F. Yu, *J. Am. Chem. Soc.*, 2011, **94**, 3153–3170.
6 X. Jiang, K. Kim, S. Zhang, J. Johnson and G. Salazar, *Sensors*, 2014, **14**, 144–169.
7 D. Damjanovic, N. Klein and V. Porokhonskyy, *Funct. Mater. Lett.*, 2010, **3**, 5–13.
8 A. Garg and D. Agrawal, *Mater. Sci. Eng., B*, 2001, **86**, 134–143.
9 J. Rödel, W. Jo, K. T. P. Seifert, E.-M. Anton, T. Granzow and D. Damjanovic, *J. Am. Ceram. Soc.*, 2009, **92**, 1153–1177.
10 J. Rödel, K. G. Webber, R. Dittmer, W. Jo, M. Kimura and D. Damjanovic, *J. Eur. Ceram. Soc.*, 2015, **35**, 1659–1681.
11 A. J. Bell and O. Deubzer, *MRS Bull.*, 2018, **43**, 581–587.
12 R. E. Eitel, C. A. Randall, T. R. Shrout, P. W. Rehrig, W. Hackenberger and S.-E. Park, *Jpn. J. Appl. Phys.*, 2001, **40**, 5999.
13 V. Goldschmidt, *Naturwissenschaften*, 1926, **14**, 477–485.
14 C. A. Bridges, M. Allix, M. R. Suchomel, X. Kuang, I. Sterianou, D. C. Sinclair and M. J. Rosseinsky, *Angew. Chem., Int. Ed.*, 2007, **46**, 8785–8789.
15 T. Rowe, B. N. Richtik and M. Dolgos, *Adv. Electron. Mater.*, 2023, **9**, 2200910.
16 M. Dolgos, U. Adem, X. Wan, Z. Xu, A. J. Bell, T. P. Comyn, T. Stevenson, J. Bennett, J. B. Claridge and M. J. Rosseinsky, *Chem. Sci.*, 2012, **3**, 1426–1435.
17 X. Zhou, J. Zhang, H. Luo, Y. Zhang, S. Tang, H. Huang, X. Yuan, M. Song, H. Qi and D. Zhang, *Nat. Commun.*, 2024, **15**, 6625.
18 S. O. Leontsev and R. E. Eitel, *J. Mater. Res.*, 2011, **26**, 9–17.
19 B. N. Richtik, A. Manjón-Sanz and M. Dolgos, *Acta Crystallogr., Sect. B:Struct. Sci., Cryst. Eng. Mater.*, 2025, **81**, 337–349.
20 H. Zheng, I. M. Reaney, W. E. Lee, N. Jones and H. Thomas, *J. Am. Ceram. Soc.*, 2002, **85**, 2337–2344.
21 J. L. Jones, *J. Electroceram.*, 2007, **19**, 69–81.
22 T.-M. Usher-Ditzian, I. Levin, J. Daniels and J. Jones, *Sci. Rep.*, 2015, **5**, 14678.
23 A. J. Goetzee-Barral, T.-M. Usher, T. J. Stevenson, J. L. Jones, I. Levin, A. P. Brown and A. J. Bell, *Phys. Rev. B*, 2017, **96**, 014118.
24 C. Zhao, D. Hou, C.-C. Chung, Y. Yu, W. Liu, S. Li and J. L. Jones, *J. Appl. Phys.*, 2017, **122**, 174102.
25 C. Zhao, D. Hou, C.-C. Chung, H. Zhou, A. Kynast, E. Hennig, W. Liu, S. Li and J. L. Jones, *Acta Mater.*, 2018, **158**, 369–380.
26 A. Manjón-Sanz, C. M. Culbertson, D. Hou, J. L. Jones and M. R. Dolgos, *Acta Mater.*, 2019, **171**, 79–91.
27 D. A. Keen, *Crystallogr. Rev.*, 2020, **26**, 143–201.
28 K. Page, T. Proffen, M. Niederberger and R. Seshadri, *Chem. Mater.*, 2010, **22**, 4386–4391.
29 M. S. Senn, D. A. Keen, T. C. A. Lucas, J. A. Hriljac and A. L. Goodwin, *Phys. Rev. Lett.*, 2016, **116**, 207602.
30 C. A. Schneider, W. S. Rasband and K. W. Eliceiri, *Nat. Methods*, 2012, **9**, 671–675.
31 B. H. Toby and R. B. Von Dreele, *J. Appl. Crystallogr.*, 2013, **46**, 544–549.
32 E. Lorch, *J. Phys. C:Solid State Phys.*, 1969, **2**, 229.
33 L. Lutterotti, R. Vasin and H.-R. Wenk, *Powder Diffr.*, 2014, **29**, 76–84.
34 D. Balzar and N. Popa, *Thin Solid Films*, 2004, **450**, 29–33.
35 I. Levin, V. Krayzman, J. C. Woicik, F. Bridges, G. E. Sterbinsky, T.-M. Usher, J. L. Jones and D. Torrejon, *Phys. Rev. B*, 2016, **93**, 104106.
36 K. V. Lalitha, C. M. Fancher, J. L. Jones and R. Ranjan, *Appl. Phys. Lett.*, 2015, **107**, 052901.
37 J. L. Jones, E. B. Slamovich and K. J. Bowman, *J. Appl. Phys.*, 2005, **97**, 034113.
38 J. L. Jones, M. Hoffman and K. J. Bowman, *J. Appl. Phys.*, 2005, **98**, 024115.
39 M. R. Rowles and C. E. Buckley, *J. Appl. Crystallogr.*, 2017, **50**, 240–251.
40 R. Eitel and C. A. Randall, *Phys. Rev. B:Condens. Matter Mater. Phys.*, 2007, **75**, 094106.
41 G. Tutuncu, B. Li, K. Bowman and J. L. Jones, *J. Appl. Phys.*, 2014, **115**, 144104.
42 Y. M. Jin, Y. U. Wang, A. G. Khachaturyan, J. F. Li and D. Viehland, *J. Appl. Phys.*, 2003, **94**, 3629–3640.
43 D. K. Khatua, L. K. Venkataraman, C. M. Fancher, J. L. Jones and R. Ranjan, *Phys. Rev. B*, 2016, **93**, 104103.
44 G. Tutuncu, J. Chen, L. Fan, C. M. Fancher, J. S. Forrester, J. Zhao and J. L. Jones, *J. Appl. Phys.*, 2016, **120**, 044103.
45 G. Tutuncu, L. Fan, J. Chen, X. Xing and J. L. Jones, *Appl. Phys. Lett.*, 2014, **104**, 132907.
46 H. Liu, S. Sun, Z. Pan, L. Fan, Y. Ren, X. Xing and J. Chen, *J. Eur. Ceram. Soc.*, 2019, **39**, 5277–5284.
47 Z. Yu, F. Su, A. Tian, X. Xie, Z. Xu, J. Fu and R. Zuo, *Acta Mater.*, 2025, **283**, 120580.

48 J. Fu, Z. Yu, A. Xie, Z. Yu, Z. Fu, X. Jiang, T. Li and R. Zuo, *Acta Mater.*, 2023, **254**, 118991.
49 J. E. Daniels, W. Jo, J. Rödel and J. L. Jones, *Appl. Phys. Lett.*, 2009, **95**, 032904.
50 M. Hinterstein, J. Rouquette, J. Haines, P. Papet, M. Knapp, J. Glaum and H. Fuess, *Phys. Rev. Lett.*, 2011, **107**, 077602.
51 A. Pramanick, D. Damjanovic, J. E. Daniels, J. C. Nino and J. L. Jones, *J. Am. Ceram. Soc.*, 2011, **94**, 293–309.
52 T.-M. Usher, J. S. Forrester, M. McDonnell, J. Neuefeind, K. Page, P. F. Peterson, I. Levin and J. L. Jones, *Rev. Sci. Instrum.*, 2018, **89**, 092905.
53 Y. Yao, H. Liu, Y. Hu, K. Datta, J. Wu, Y. Zhang, M. G. Tucker, S. Liu, J. C. Neuefeind, S. Zhang and J. Chen, *Nat. Commun.*, 2025, **16**, 7442.
54 S. Y. Chong, R. J. Szczecinski, C. A. Bridges, M. G. Tucker, J. B. Claridge and M. J. Rosseinsky, *J. Am. Chem. Soc.*, 2012, **134**, 5836–5849.